Virtual pulse reconstruction diagnostic for single-shot measurement of free electron laser radiation power

Till Korten[®], ¹ Vladimir Rybnikov[®], ² Peter Steinbach[®], ¹ and Najmeh Mirian[®], ^{*} ¹ Helmholtz-Zentrum Dresden-Rossendorf (HZDR), Dresden 01328, Germany ² Deutsches Elektronen-Synchrotron (DESY), Hamburg 22607, Germany

(Received 26 November 2024; accepted 28 February 2025; published 25 March 2025)

Accurate characterization of radiation pulse profiles is crucial for optimizing beam quality and enhancing experimental outcomes in free electron laser (FEL) research. In this paper, we present a unique approach that employs machine learning techniques for real-time virtual diagnostics of FEL radiation pulses. Our simple artificial intelligence (AI)-based diagnostic tool utilizes longitudinal phase space data obtained from the X-band transverse deflecting structure to reconstruct the temporal profile of FEL pulses in real time. Unlike traditional single-shot methods, this AI-driven solution provides a noninvasive, highly efficient alternative for pulse characterization. By leveraging state-of-the-art machine learning models, our method facilitates precise, single-shot measurements of FEL pulse power, offering significant advantages for FEL science research. This work outlines the conceptual framework, methodology, and validation results of our virtual diagnostic tool, demonstrating its potential to significantly impact FEL research.

DOI: 10.1103/PhysRevAccelBeams.28.030703

I. INTRODUCTION

In recent years, electron beam accelerators have become essential in fields such as medical therapies, materials science, and particle physics research. Their successful operation relies on the precision and stability of the electron beam, which requires advanced diagnostic technologies to monitor and maintain beam quality. Traditional diagnostic methods, while effective, often struggle with the complex, dynamic nature of electron beams. This is where machine learning (ML) emerges as a transformative technology, elevating diagnostic capabilities by providing enhanced precision, adaptability, and efficiency (Scheinker et al. [1], Edelen et al. [2], Sanchez-Gonzalez et al. [3], Ratner [4], Kaiser et al. [5,6], Fujita [7], Emma et al. [8], and Dingel et al. [9]). Machine learning algorithms excel at processing and analyzing vast amounts of data from diagnostic sensors and instruments with unprecedented speed and accuracy. These algorithms can identify patterns and anomalies that might indicate issues with the beam or the accelerator components. For instance, ML models can be trained on archived (history) data to recognize normal operating parameters of an electron beam. By continuously

Published by the American Physical Society under the terms of the Creative Commons Attribution 4.0 International license. Further distribution of this work must maintain attribution to the author(s) and the published article's title, journal citation, and DOI. monitoring real-time data, these models can quickly detect deviations from the norm, signaling potential issues before they escalate [10–12].

The integration of machine learning into diagnostic technology brings numerous advantages: enhanced precision, real-time analysis, adaptability, and data-driven insights. ML algorithms enable highly accurate detection and monitoring of beam characteristics, ensuring precision in diagnostics. The real-time data processing capabilities of ML models allow for the immediate identification of issues and swift corrective actions. Additionally, while machine learning systems adapt to new data, their ability to respond to evolving conditions is still an active area of research, offering a flexible solution for the dynamic nature of electron beams [13,14]. Moreover, ML-driven diagnostics provide deeper insights into accelerator behavior and performance, facilitating informed decision making and optimization strategies [1-3]. As machine learning continues to evolve, its expanding role in the diagnostic technology of electron beam accelerators is gradually transforming the field of accelerator diagnostics and control systems. By improving the precision, reliability, and efficiency of diagnostic processes, ML contributes significantly to the optimal performance and longevity of these complex systems. As these technologies evolve, their impact on diagnostic applications is expected to expand, driving further innovations and enhancements in electron beam accelerator operations [8,15-20].

Building on decades of advancements in accelerator technology, including significant progress in hardware and

^{*}Contact author: najmeh.mirian@hzdr.de

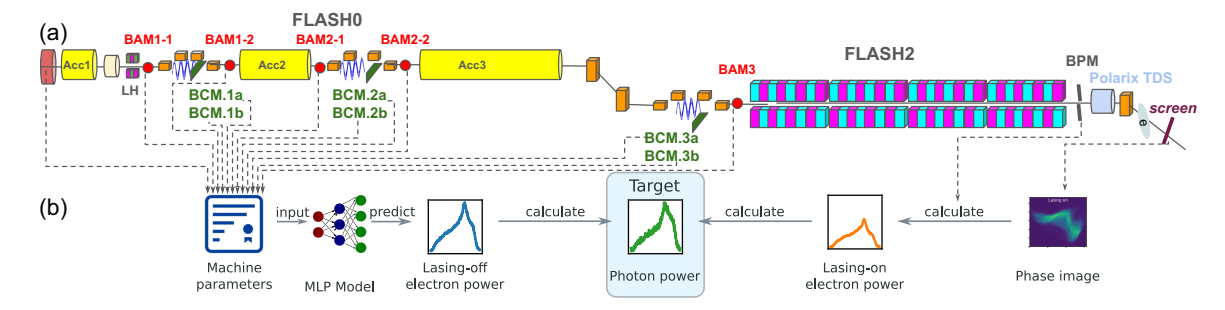


FIG. 1. (a) Schematic layout of the FLASH0 (injector and accelerator) and the FLASH2 beamline at DESY. Data sources for training the machine learning model are indicated by dashed arrows. (b) Process workflow. During machine operation, we measured machine parameters and the longitudinal phase space (phase image) for each electron bunch. We use a multilayer perceptron machine learning model (MLP model) to predict the temporal power profile of the electron bunch in the lasing-off condition (lasing-off e-beam power). From the longitudinal phase space, we calculate the temporal power profile of the electron bunch in the lasing-on condition (lasing-on e-beam power). Thus, we can estimate the temporal power profile of each individual photon pulse (photon power).

software, free electron lasers (FELs) have revolutionized the generation of highly coherent, powerful electromagnetic radiation at subatomic wavelengths. Innovations in electron accelerators now enable FELs to produce intense, ultrashort pulses, spanning from extreme ultraviolet to hard x-rays at exceptionally high repetition rates. These FELs, powered by high-brightness electron beams, have opened up new possibilities for exploring molecular and atomic dynamics, with profound implications across fields such as physics, chemistry, biology, medical physics, and materials science. The ability to generate coherent, powerful, and ultrashort pulses in the shortwavelength regime has become crucial for advancing research in these domains [21–25].

To analyze FEL experimental data, especially for nonlinear interactions, it is essential to have precise knowledge of the FEL pulse peak power and the electric field in the time domain. Conducting pulse-to-pulse measurements of the x-ray pulse structure over time could pave the way for new scientific discoveries, such as the ability to study ultrafast dynamics in materials or biological systems. For example, the use of single-shot x-ray pulse measurements has already enabled groundbreaking insights into the behavior of matter under extreme conditions, as seen in studies conducted at the European XFEL [26-28]. Such measurements are critical for understanding time-resolved phenomena at the atomic scale. For instance, more powerful x-ray analogs of optical nonlinear spectroscopies, such as x-ray absorption spectroscopy or x-ray pump-probe techniques, and resolution-limited standard pump-probe experiments, would greatly benefit from precise knowledge of the FEL radiation's electric field. Such measurements can improve temporal resolution and enable the study of ultrafast processes at atomic and molecular levels, as demonstrated in studies using x-ray FELs like those at the European XFEL [26,28]. This enhanced understanding of the FEL pulse structure could also pave the way for novel applications in material science and biological imaging [29–37].

To achieve the precision required in FEL experiments, various diagnostic methods have been developed. One such method is the transverse reconstruction of the electron beam and x-ray algorithm, which aims to reconstruct the temporal power profile P(t) by analyzing the product of the measured current profile and the difference between the energy spread or mean energy profiles of lasing-on and lasing-off shots using a transverse deflecting cavity (TDS) (see Fig. 1 in [38]). However, this approach is constrained by the finite resolution of the TDS [39], and it is also impossible to simultaneously measure the lasing-on and lasing-off electron phase spaces for a single shot [18,40].

To overcome the single-shot measurement challenges, we introduce the virtual pulse reconstruction diagnostic (VPuRD), a novel tool designed to reconstruct or measure the FEL pulse on a shot-to-shot basis. VPuRD leverages advanced machine learning (ML) techniques to bypass the cumbersome limitations associated with traditional methods of single-shot phase space measurements. Typically, the process involves turning off the lasing for each measurement and capturing the longitudinal phase space across multiple electron beam shots, which is both time consuming and invasive [38]. The VPuRD tool addresses this by employing ML models to reconstruct the longitudinal phase space of the electron beam using parameters derived from noninvasive diagnostic tools. This innovation enables our virtual diagnostic tool to accurately reconstruct the FEL pulse for each individual electron beam, providing a more efficient and precise measurement process. By eliminating the need for repeated lasing-off measurements, VPuRD not only simplifies the diagnostic procedure but also enhances the accuracy and reliability of FEL pulse characterization. To demonstrate the applications and advantages of our VPuRD tool, we selected the Free electron LASer in Hamburg (FLASH), a state-of-the-art facility located at Deutsches Elektronen-Synchrotron (DESY) in Germany. In the following section, we will discuss the facility and hardware tools utilized for our measurements. The subsequent sections will be dedicated to the methodology, discussion, and results of our virtual diagnostic tool.

II. FACILITY, HARDWARE AND SOFTWARE A. FLASH

FLASH is a free-electron laser machine that generates extremely bright, ultrashort pulses of laser light in the ultraviolet and soft x-ray regions of the electromagnetic spectrum. This unique capability makes FLASH an invaluable tool for researchers across a wide range of scientific disciplines, including physics, chemistry, biology, and materials science [41,42]. FLASH is a high-repetition facility at 1 MHz in burst mode, i.e., offers the ability to deliver a burst of 500 electron bunches in each 0.1 s. FLASH operates by accelerating a train of electron bunches using a superconducting linear accelerator (Linac). These high-energy electrons are then directed through a series of undulator magnets, whose magnetic structures force the electrons to follow a sinusoidal path, causing them to emit synchrotron radiation. Through a process known as selfamplified spontaneous emission (SASE), this radiation is amplified to produce intense, coherent laser pulses. FLASH has two undulator magnet chains, referred to as FLASH1 and FLASH2.

Figure 1 shows the layout of the common FLASH0 (injector and accelerator) and the FLASH2 FEL beamline. The accelerator section includes two bunch compressor sections, BC1 and BC2, each with two bunch compressor monitor systems (BCMs) and two bunch arrival time monitors (BAMs) at the entrance and exit of the bunch compressors [43–48]. The FLASH2 line features an additional bunch compressor, allowing for further compression of the electron beam, and includes two BCM systems along with one BAM.

The bunch compressor monitor at FLASH, utilizing the detection of coherent diffraction radiation, is a noninvasive diagnostic tool essential for monitoring electron bunch compression to achieve the desired length and properties. For accurate measurements, the BCM system often incorporates diagnostic components such as pyroelectric detectors and filters, which are specifically sensitive to infrared radiation. These detectors and filters are optimized to match the spectral range of the coherent diffraction radiation emitted, which depends on the beam energy and bunch lengths at each stage of compression. Pyroelectric detectors in the BCMs converts changes in temperature caused by absorbed electromagnetic radiation (primarily in the infrared spectrum) into electrical signals. This signal is proportional to the intensity of the coherent radiation. Filters and amplifiers are typically used to isolate the relevant frequency range, which corresponds to the spectral region of interest for the bunch compression stage. By analyzing the intensity of detected signals, the BCM provides real-time information about the compression state of the electron bunch. Changes in signal amplitude indicate variations in bunch length and compression efficiency. The FLASH machine employs both more sensitive and less sensitive pyroelectric detectors within its BCM systems, allowing for enhanced measurement capabilities and improved control over the electron bunch compression process. More details about the BCM setups at FLASH have been presented in [44–46].

The bunch arrival monitor (BAM) is also a noninvasive diagnostic tool used to measure the entry and exit times of electron bunches. The longitudinal dispersion in the bunch compression chicanes correlates changes in beam energy upstream of the chicane with arrival time changes downstream of the bunch compressor. In other words, for a given fixed machine setup, the BAM measures the relative energy of the beam during the run. The data acquisition (DAQ) system in our virtual diagnostic setup collects shot-to-shot data from the BAMs and BCMs, as well as the charge and energy of the electron beam at the end of the Linac. The following two sections will discuss our DAQ system in detail.

One of the most notable features of FLASH is its capability to generate extremely short pulses, on the order of femtoseconds (10^{-15} s), particularly in the FLASH2 undulator line [49]. These ultrashort pulses allow researchers to study phenomena occurring on extremely fast timescales, such as the dynamics of chemical reactions and electron behavior in materials. Users of the FLASH2 beamline are often interested in the FEL pulse profile [50]. To a certain extent, this need is addressed by a feature of the variable-polarization X-band transversely deflecting structure (POLARIX TDS) downstream of the FLASH2 undulator line [51]. This device enables pulse reconstruction of the FEL through the transverse reconstruction of the electron beam and x-ray algorithm [52]. We will explore the POLARIX TDS and its role in our virtual diagnostic in detail in a separate subsection.

B. POLARIX TDS

The POLARIX TDS is an advanced device that plays a crucial role in the detailed characterization of the electron bunches produced by the FLASH facility. It provides valuable insights into the temporal and spatial properties of these ultrafast electron beams. POLARIX operates at a specific radio frequency (rf), with almost 12 GHz frequency that is synchronized with the electron bunches passing through it [53–56]. The frequency is carefully chosen to match the operational parameters of FLASH2. The cavity generates an electromagnetic field that imparts a transverse momentum to the electrons. Both the strength (rf voltage) and direction (rf phase) of this deflection are meticulously controlled to achieve the desired temporal-tospatial mapping. This mapping allows for measurements of bunch length and temporal distribution at a resolution of the order of femtoseconds. The device plays a crucial role in optimizing FLASH's performance [51]. Consequently, the POLARIX TDS is integral to our virtual diagnostic tool. During data collection, we gather information on the POLARIX TDS rf phase, rf voltage, electron beam energy, charge, and the position of the electron both before and after the TDS cavity. Additionally, the longitudinal phase space of the electron beam is captured by the YAG screen located after the bending magnet positioned downstream of the TDS cavity (see Fig. 1). During data acquisition, the time calibration factor was 1.13 fs/mm and energy calibration factor was 21 keV/mm. By considering the transverse electron beam spot size, the time resolution was 15.4 fs in our measurements.

C. Data acquisition system

The fast data acquisition system (DAQ) [57] of the FLASH control system has been used in our virtual diagnostic. The DAQ system was developed to study, monitor, and document the machine performance and parameters and also to collect the results of the experiment measurements at FLASH. The DAQ data (machine parameters) are collected in real time with the unique identification for each shot in the Linac coming from the FLASH timing system. In this way, one can easily correlate any diagnostics DAQ channel data at the bunch-by-bunch level. The collected data can be processed both on and off-line. The first approach is used by the slow feedback middle layer servers. The second approach makes use of the DAQ data raw files written during the data collection. The DAQ files are written in a highly optimized custom format. For our virtual diagnostics the raw files were converted to HDF5 files.

III. METHODOLOGY

Machine learning (ML) methods are increasingly being employed to enhance the accuracy of longitudinal phase space measurements of electron beams in FELs like FLASH2 at DESY. These techniques provide sophisticated tools to analyze complex data and improve the precision of measurements, which are critical for optimizing the performance of FELs [20].

We collected data while the FLASH machine was optimized for FEL radiation for user delivery. The electron beam, with a charge of 200 pC, was accelerated to an energy of 875 MeV, allowing the FLASH2 beamline to generate FEL radiation at 12 nm. In the lasing-off condition, FEL radiation was suppressed by deflecting the electron beam trajectory at the entrance of the undulator line.

For virtual pulse reconstruction, we employed the following workflow (see Fig. 1): For each electron bunch, the DAQ system collected 23 machine parameters (as shown in Table I) along with a longitudinal phase space image. These machine parameters were used as inputs to predict the shape of the temporal power profile of the

TABLE I. Machine parameters used as model input.

| Parameter name | Definition |
|----------------------------|---|
| BCM.1a | Measured data from more sensitive |
| | pyroelectric detector after BC1 |
| norm. BCM.1a | Normalized BCM.1a to the bunch charge |
| BCM.1b | Measured data from less sensitive pyroelectric detector in BC1 |
| norm. BCM.1b | Normalized BCM.1b to the bunch charge |
| BCM.2a | Measured data from more sensitive pyroelectric detector after BC2 |
| norm. BCM.2a | Normalized BCM.2a to the bunch charge |
| BCM.2b | Measured data from less sensitive pyroelectric detector after BC2 |
| norm. BCM.2b | Normalized BCM.2b to the bunch charge |
| BCM.3a | Measured data from more sensitive pyroelectric detector in FLASH2 after BC3 |
| norm. BCM.3a | Normalized BCM.3a to the bunch charge |
| BCM.3b | Measured data from less sensitive pyroelectric detector in FLASH2 after BC3 |
| norm. BCM.3b | Normalized BCM.3b to the bunch charge |
| BAM1-1 | Bunch arriving time before BC1 |
| BAM1-2 | Bunch exciting time after BC1 |
| BAM2-1 | Bunch arriving time before BC2 |
| BAM2-2 | Bunch exciting time after BC2 |
| BAM3 | Bunch arriving time before BC3 |
| Δt (BAM1-2-BAM1-1) | Time delay at BC1 |
| Δt (BAM2-2-BAM2-1) | Time delay at BC2 |
| CHARGE | Electron bunch charge generated at electron |
| in gun | gun |
| CHARGE in FLASH2 | Electra bunch charge at FLASH2 beamline |
| ENERGY in FLASH2 | Electron beam energy |
| BPM x , y | Electron beam position before TDS in <i>x</i> and <i>y</i> directions |

electron bunch in the lasing-off condition. The temporal power profile of the electron beam in the lasing-on condition was measured directly from the longitudinal phase space. Consequently, we were able to reconstruct the temporal radiation power profile for each individual photon pulse.

Here, we focus on the machine learning part. Toward this end, we develop a multilayer perceptron (MLP) machine learning model that is able to predict the temporal power profile of the electron bunch in the lasing-off condition. Toward this end, we collect the machine parameters as well as the longitudinal phase space for 2826 electron bunches in the lasing-off condition as training data.

A. Data collection and preprocessing

We collect 23 machine parameters detailed in Table I. Each parameter is a scalar that corresponds to a measurement at a specific point of the beamline. A precision timing

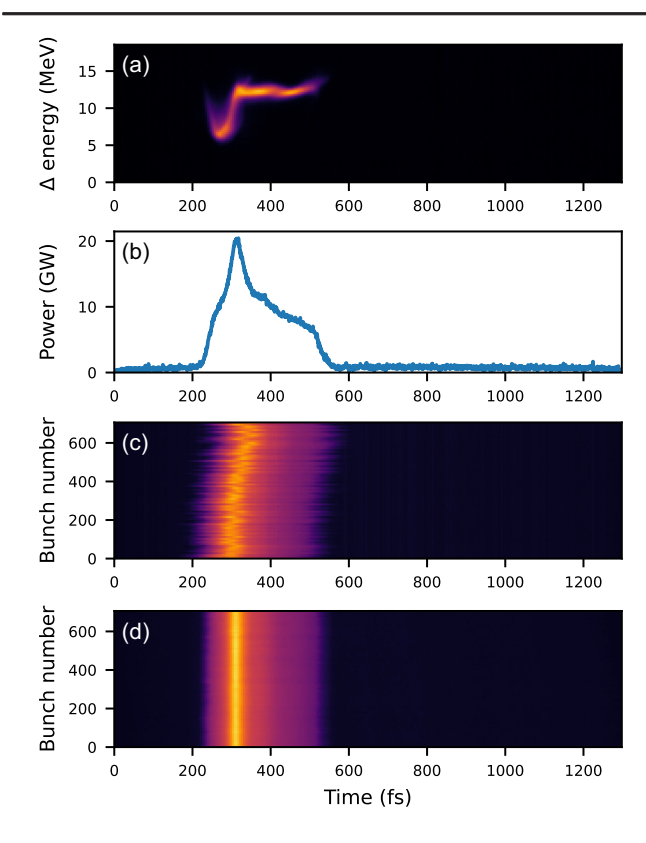


FIG. 2. Dejittering. (a) Electron beam phase space image. (b) Temporal power profile created by weighting the phase image by the energy axis and projecting it onto the time axis. (c) Temporal power profiles of 700 samples before dejittering. (d) Temporal power profiles after dejittering.

system is used to assign individual measurements to specific electron bunches. High-resolution data on the electron beam's longitudinal phase space, collected by POLARIX TDS at 10 Hz [Fig. 2(a)], are preprocessed to remove noise, background, and irrelevant information.

1. Jittering

The jitter observed in the electron bunch longitudinal phase space data [Fig. 2(a)] originates from POLARIX radio-frequency (rf) phase jitters. Accurately calculating the FEL pulse power profile from longitudinal phase space data necessitates precise alignment of the electron beam power profiles for lasing-on and lasing-off conditions. This alignment is critical because the FEL power profile is derived as the difference between these two electron beam profiles.

To compensate for jitter in the electron bunch longitudinal phase space [Fig. 2(c)] we employed a datacleaning procedure to align the images and mitigate its impact on the calculated FEL pulse power profile. In our case, since the jitter predominantly originates from rf phase fluctuations in the deflecting cavity, our approach effectively compensates for this artifact, ensuring accurate reconstruction. We calculate the electron temporal power

profile for each electron bunch [examples shown in Figs. 2(a) and 2(b)]. The electron bunches show notable temporal jitter [Fig. 2(c)]. To compensate for the jitter, the peak power locations are determined from power profiles smoothed by convolving the signal with a Gaussian profile with 10 pixel radius. Then, we calculate the offset of each peak to the median peak location and shift the power profiles accordingly, resulting in a proper alignment [Fig. 2(d)]. Finally, we crop away the parts of the signal that only contain background in every bunch. The location of the signal is determined by segmenting the signal using Otsu's method [58] and cropping to the bounding box of the segmentation with a padding of 50 pixels. The aligned power profiles are used as labels for the training of the MLP model. Image processing was performed using pyclesperanto, a GPU-accelerated Python library for image analysis [59,60].

2. Temporal power profile

The electron temporal power profile is calculated from the charge detected in each slice of the longitudinal phase space image [Fig. 2(a)], multiplied by the corresponding energy difference (Δ energy) in MeV. The resulting energy weighted charge is projected onto the time axis to calculate the electron temporal power profile [Fig. 2(b)].

B. Model training and validation

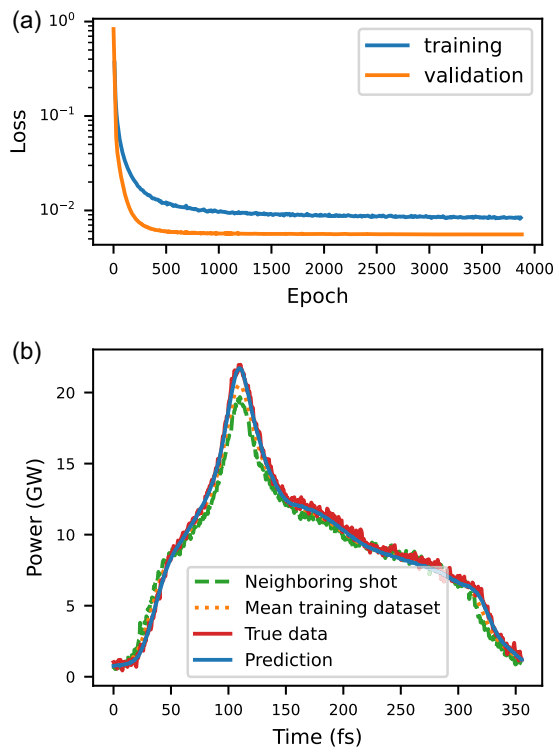
We use a simple MLP model with 23 input nodes, one for each scalar machine parameter from the beamline (see Table I for details on the input parameters), a single hidden layer with 295 nodes, and an output layer with 567 nodes (the width of the electron temporal power profiles in the training data). The 2826 datasets are split into training, validation, and test sets with 2261, 283, and 282 samples, respectively.

We use an adapted loss function that penalizes regression to the mean:

$$L = \sum_{i=1}^{D} (x_i - y_i)^2 - \alpha \sum_{i=1}^{D} (x_i - \hat{y})^2,$$
 (1)

where \hat{y} is the mean vector of the label vectors of the entire training dataset, α is a penalty factor, which we set to 0.056, x_i are the prediction vectors, and y_i are the respective label vectors.

Hyperparameters are optimized with optuna [61] using 200 trials. After optimization, a model with one hidden layer is trained in Pytorch [62] using the Adam optimizer [63], a dropout fraction of 0.45 on the hidden layer, an initial learning rate of 0.005, a learning rate scheduler with a factor of 0.054 and a patience of 238. Training is stopped using the EarlyStopping callback from Pytorch Lightning [64] with a patience of 1225. To improve GPU utilization, we use single batch training, training



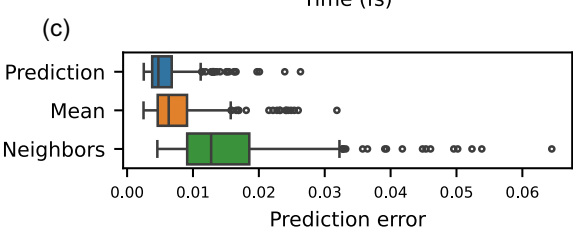


FIG. 3. MLP model training performance. (a) Training and validation loss. (b) Illustrative example of electron power profiles from the test dataset: Predictions for individual shots (blue line), actual measurements (red line), measurements from previous shot (dashed green line); as well as the mean electron power profile of all measurements in the training data (dotted orange line). (c) Boxplots of all mean squared errors in the test dataset: Mean squared error between the predictions and the measurements in the test dataset (prediction). Mean squared error between the measurements in the training dataset (mean). Mean squared error between adjacent measurements in the test dataset (neighbors). All three errors are statistically significantly different from each other (Wilcoxon signed-rank test [65] followed by a Bonferroni correction [66] for multiple comparisons).

the model on the entire training dataset. Training and validation losses converge well with no indication of overfitting [Fig. 3(a)].

IV. RESULTS AND DISCUSSION

A. Prediction results

Predicted temporal electron beam power profiles matched the measured profiles very well [Fig. 3(b) blue

line vs red line]. Because of the penalty for predictions that were too close to the mean in the loss function [Eq. (1)], the model did not simply regress to the mean of the training dataset [Fig. 3(b) orange dotted line]. Notably, the neighboring measurement [Fig. 3(b) green dashed line] fit the measurement even worse than the mean of all shots. These individual observations exemplified in [Fig. 3(b)] are confirmed by plotting the mean squared errors for all samples in the test dataset [Fig. 3(c)]. The predictions have the lowest mean squared error compared to the measurements in the test dataset $[0.009 \pm 0.0050]$ (mean \pm standard deviation, n = 282)]. This is better than the mean squared error between the mean of the entire training dataset and the individual measurements in the test dataset (0.011 ± 0.007) . The highest mean squared error was observed between neighboring measurements and can be approximated as:

$$\frac{\sum (x_i - x_{i+1})^2}{n-1},\tag{2}$$

where x_i are the individual measurements and n is the total number of measurements. In the test dataset (0.02 ± 0.014) , all three errors are statistically significantly different from each other (p < 0.01) as determined by a one-way analysis of variance (ANOVA) followed by Tukey's HSD test [67]. The observation that neighboring measurements are not good predictors is significant, because neighboring shots have previously been used as labels to train machine learning models to predict longitudinal phase space data [20].

B. Photon power reconstruction

We apply the model, trained on 2261 shots in the lasing-off condition, to 574 shots acquired in the lasing-on condition (Fig. 4). The model predicted electron beam powers in the lasing-off condition [blue line in Fig. 4(a)]. By subtracting the measured electron beam power in the lasing-on condition [red line in Fig. 4(a) and Eq. (3)], we were able to reconstruct the photon pulse power profile [Fig. 4(b)]. Photon power was calculated as:

$$p_{\nu} = p_{\text{eoff}} - p_{\text{eon}},\tag{3}$$

where p_{ν} is the photon power profile vector, $p_{\rm eoff}$ is the electron power profile vector in the lasing-off condition, and $p_{\rm eon}$ is the electron power profile vector in the lasing-on condition. This shot-to-shot reconstruction is compatible with the state-of-the-art reconstruction method based on averaging the datasets from both the lasing-off and lasing-on conditions [Figs. 4(c) and 4(d)]. As displayed in this figure, the electron beam power in the lasing-on condition in the 80–120 fs time range is larger than in the lasing-off condition. In pulse reconstruction, this effect results in negative FEL radiation power, which needs to be removed

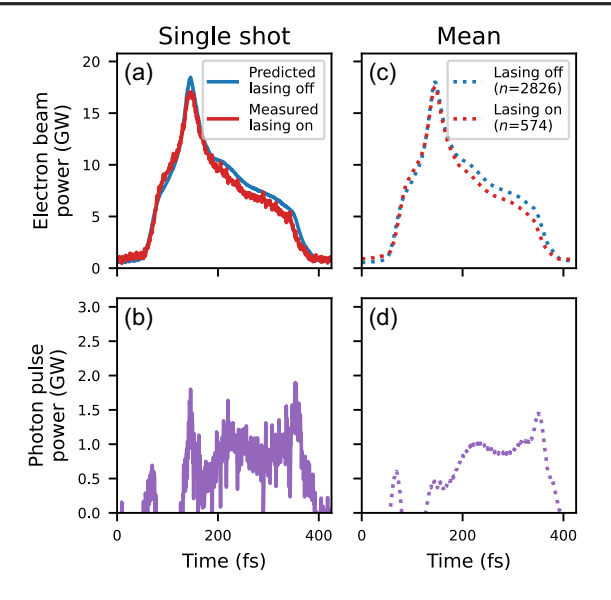


FIG. 4. Single shot vs mean photon power reconstruction. (a) Electron beam power for one example shot. Electron beam power in the lasing-off condition (blue line) is predicted by the model and electron beam power in the lasing-on condition (red line) is measured. (b) Reconstructed photon pulse power for the same shot as in (a). (c) Mean electron beam power from 2826 shots from the lasing-off condition (blue dotted line) and 574 shots from the lasing-on condition (red dotted line). (d) Mean photon pulse power calculated from (c).

for accurate analysis. This indicates that electrons in this part of the bunch are absorbing FEL radiation, likely due to the slippage effect and phase mismatch. While the electrons travel through the undulator line, the high-power FEL radiation generated by the peak current slips (around 170 fs) onto the head of the electron beam. A portion of this radiation can be absorbed by the electrons, and part of it is observed as FEL radiation at the head of the beam. This phenomenon is evident in the results of both methods. This introduces an uncertainty in the reconstructed pulse's head, though it is explainable and consistent with the slippage mechanism.

The temporal spike structure in the SASE (self-amplified spontaneous emission) spectrum is a well-known characteristic [68]. These spikes result from the stochastic nature of the initial electron beam density modulations that amplify through the undulator. The length of each spike in the time domain (or the spike width) is determined by the coherence time of the FEL radiation. This coherence time, τ_c , is inversely proportional to the spectral bandwidth $\Delta\omega$ of the SASE radiation $\tau_c \approx 1/\Delta \omega$. For typical x-ray SASE FELs, such as FLASH, this coherence time (and hence the duration of each temporal spike) is in the range of femtoseconds, often between one fs and a few tens fs depending on the wavelength and specific machine parameters. At shorter wavelengths, the spikes tend to be narrower, while at longer wavelengths, they can be somewhat broader. In our measurements, FLASH2 was operated at a wavelength

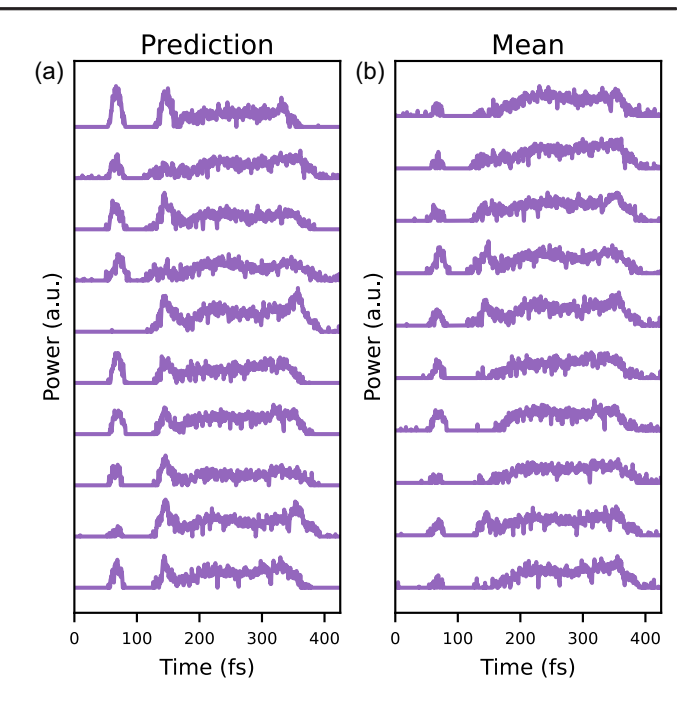


FIG. 5. Multiple examples of single-shot photon power reconstruction. (a) Photon powers reconstructed from data predicted by the machine learning model [calculated as for Fig. 4(b)]. (b) Photon powers reconstructed by subtracting the same measured lasing-on profiles as in (a) from the mean of 2261 shots from the lasing-off condition.

of 12 nm, producing temporal spikes of only a few femtoseconds each [68], which is shorter than the 15.4 fs resolution of POLARIX. This makes it challenging to capture the temporal spike structure of the SASE FEL pulse using this method. The overall accuracy of both arms of the reconstruction (laser-on and laser-off prediction) depends on the resolution of longitudinal phase space measurements obtained from the transverse deflecting cavity.

Figure 5 illustrates ten single-shot FEL pulse reconstructions measured using VPuRD at the FLASH control system. The results are shown for two approaches in plots (a) and (b). In both methods, a single shot of the electron beam phase space in the lasing-on condition was used to directly evaluate the beam power. In Fig. 5(a), a machine learning-based method was employed to predict the electron beam power for the lasing-off condition for each FEL shot. In Fig. 5(b), the mean values from 2261 shots were used to evaluate the electron beam power for the lasing-off condition. The machine learning method in VPuRD facilitates the reconstruction of FEL pulses, making the process more efficient and accessible.

While the VPuRD tool has demonstrated its capability for FEL pulse characterization, it faces a specific challenge that requires consideration. During data collection in the lasing-off condition, the SASE radiation was suppressed by deflecting the electron beam trajectory at the entrance of the undulator line. This approach introduced betatron oscillations and slightly shifted the position of the electron beam on the energy axis. To address this issue, we compensated for the error using energy measurement data obtained near the screen ($\Delta_{\rm energy}=1.35$ MeV). In the future, we plan to implement trajectory feedback to correct the beam trajectory after the undulator line. Alternatively, data could be collected by detuning the undulator's resonance condition, which may help mitigate this challenge more effectively.

Additionally, it should be noted that slippage presents another challenge for the VPuRD tool. Due to the significant slippage associated with FEL radiation at longer wavelengths, VPuRD tends to provide more accurate results for FEL radiation at shorter wavelengths.

V. CONCLUSION

This paper introduces the virtual pulse reconstruction diagnostic (VPuRD), a novel tool for single-shot reconstruction of FEL radiation power profiles. VPuRD employs a machine learning-based approach to address key challenges in traditional diagnostic methods, particularly their reliance on extensive lasing-off data. By utilizing longitudinal phase space measurements of the electron beam obtained via the X-band transverse deflection structure (TDS), VPuRD enables accurate reconstruction of temporal power profiles using only lasing-on electron beam data. This makes it a highly efficient and noninvasive diagnostic tool. Its compatibility with high-repetition-rate FEL facilities, such as FLASH, positions it as a significant innovation for real-time diagnostics. In addition to its diagnostic capabilities, VPuRD has the potential to contribute to FEL optimization and feedback systems, offering opportunities to enhance FEL performance and stability. Despite its strengths, VPuRD faces certain challenges, such as the slippage effect, which is particularly pronounced at longer wavelengths, and trajectory-induced errors. These effects can introduce uncertainties in certain parts of the reconstructed profiles, limiting the tool's applicability under specific conditions. Furthermore, the tool relies on training data that was acquired under the same conditions as the experiment in order to be able to accurately predict the lasing-off electron power profile. Addressing these challenges in future developments will further improve VPuRD's accuracy and reliability, broadening its utility for various FEL regimes.

In conclusion, VPuRD represents a significant advancement in FEL diagnostics, providing an efficient and reliable method for single-shot pulse characterization. Its implementation has the potential to streamline FEL operations, facilitate experimental success, and enable new opportunities in ultrafast science and related research fields.

Looking ahead, we plan to enhance VPuRD with additional capabilities, transforming it into a valuable tool not only for DESY but also for the broader scientific community engaged in accelerator and FEL research.

ACKNOWLEDGMENTS

The authors would like to express the gratitude to the late Siegfried Schreiber, former head of the FLASH facility, for his support and encouragement in the early stages of this project. Particular thanks go to Mathias Vogt, Juliane Roensch-Schulenburg, and Stefan Duesterer from DESY for their enlightening discussions, insightful comments, valuable suggestions, and support during FLASH operations. We also thank members of the FLASH operation team for providing help and conditions to carry out the data collection. We thank the entire teams of Helmholtz AI Matter and FLASH for invaluable discussions and a great working atmosphere.

- [1] A. Scheinker, A. Edelen, D. Bohler, C. Emma, and A. Lutman, Demonstration of model-independent control of the longitudinal phase space of electron beams in the linaccoherent light source with femtosecond resolution, Phys. Rev. Lett. **121**, 044801 (2018).
- [2] A. L. Edelen, S. G. Biedron, B. E. Chase, D. Edstrom, S. V. Milton, and P. Stabile, Neural networks for modeling and control of particle accelerators, IEEE Trans. Nucl. Sci. 63, 878 (2016).
- [3] A. Sanchez-Gonzalez *et al.*, Accurate prediction of x-ray pulse properties from a free-electron laser using machine learning, Nat. Commun. **8**, 15461 (2017).
- [4] D. Ratner, Introduction to machine learning for accelerator physics, arXiv:2006.09913.
- [5] J. Kaiser, C. Xu, A. Eichler, A. S. Garcia, O. Stein, E. Bründermann, W. Kuropka, H. Dinter, F. Mayet, T. Vinatier, F. Burkart, and H. Schlarb, Reinforcement learning-trained optimisers and Bayesian optimisation for online particle accelerator tuning, Sci. Rep. 14, 15733 (2024).
- [6] J. Kaiser, C. Xu, A. Eichler, and A. S. Garcia, Bridging the gap between machine learning and particle accelerator physics with high-speed, differentiable simulations, Phys. Rev. Accel. Beams 27, 054601 (2024).
- [7] K. Fujita, Physics-informed neural network method for space charge effect in particle accelerators, IEEE Access 9, 164017 (2021).
- [8] C. Emma, A. Edelen, M. J. Hogan, B. O'Shea, G. White, and V. Yakimenko, Machine learning-based longitudinal phase space prediction of particle accelerators, Phys. Rev. Accel. Beams 21, 112802 (2018).
- [9] K. Dingel, T. Otto, L. Marder, L. Funke, A. Held, S. Savio, A. Hans, G. Hartmann, D. Meier, J. Viefhaus, B. Sick, A. Ehresmann, M. Ilchen, and W. Helml, Artificial intelligence for online characterization of ultrashort x-ray freeelectron laser pulses, Sci. Rep. 12, 17809 (2022).
- [10] D. Marcato, G. Arena, D. Bortolato, F. Gelain, V. Martinelli, E. Munaron, M. Roetta, G. Savarese, and G. A. Susto, Machine learning-based anomaly detection for particle accelerators, in *Proceedings of the 2021 IEEE Conference on Control Technology and Applications (CCTA)* (IEEE, New York, 2021), pp. 240–246, 10.1109/CCTA48906.2021.9658806.

- [11] Y. Suetsugu, Machine-learning-based pressure-anomaly detection system for SuperKEKB accelerator, Phys. Rev. Accel. Beams 27, 063201 (2024).
- [12] D. Marcato, D. Bortolato, V. Martinelli, G. Savarese, and G. A. Susto, Time-series deep learning anomaly detection for particle accelerators, IFAC-PapersOnline **56**, 1566 (2023).
- [13] A. Scheinker, Adaptive control and machine learning for particle accelerator beam control and diagnostics, in Proceedings of the 10th International Beam Instrumentation Conference (IBIC2021), Pochang, Republic of Korea (JACoW, Geneva, Switzerland, 2021), THOB03, 10.18429/JACoW-IBIC2021-THOB03.
- [14] A. Scheinker and S. Gessner, Adaptive machine learning for time-varying systems: Towards 6d phase space diagnostics of short intense charged particle beams, arXiv: 2203.04391.
- [15] F. Cropp, L. Moos, A. Scheinker, A. Gilardi, D. Wang, S. Paiagua, C. Serrano, P. Musumeci, and D. Filippetto, Virtual-diagnostic-based time stamping for ultrafast electron diffraction, Phys. Rev. Accel. Beams 26, 052801 (2023).
- [16] O. Convery, L. Smith, Y. Gal, and A. Hanuka, Uncertainty quantification for virtual diagnostic of particle accelerators, Phys. Rev. Accel. Beams 24, 074602 (2021).
- [17] B. Marchetti *et al.*, Experimental demonstration of novel beam characterization using a polarizable x-band transverse deflection structure, Sci. Rep. 11, 3560 (2021).
- [18] A. Hanuka, C. Emma, T. Maxwell, A. S. Fisher, B. Jacobson, M. J. Hogan, and Z. Huang, Accurate and confident prediction of electron beam longitudinal properties using spectral virtual diagnostics, Sci. Rep. 11, 2945 (2021).
- [19] J. Zhu, Y. Chen, F. Brinker, W. Decking, S. Tomin, and H. Schlarb, High-fidelity prediction of megapixel longitudinal phase-space images of electron beams using encoder-decoder neural networks, Phys. Rev. Appl. 16, 024005 (2021).
- [20] J. Zhu, N. M. Lockmann, M. K. Czwalinna, and H. Schlarb, Mixed diagnostics for longitudinal properties of electron bunches in a free-electron laser, Front. Phys. 10, 903559 (2022).
- [21] S. Schreck, M. Beye, and A. Foehlisch, Implications of stimulated resonant x-ray scattering for spectroscopy, imaging, and diffraction in the regime from soft to hard x-rays, J. Mod. Opt. 62, S34 (2015).
- [22] F. Calegari, D. Ayuso, A. Trabattoni, L. Belshaw, S. De Camillis, S. Anumula, F. Frassetto, L. Poletto, A. Palacios, P. Decleva, J. B. Greenwood, F. Martín, and M. Nisoli, Ultrafast electron dynamics in phenylalanine initiated by attosecond pulses, Science 346, 336 (2014).
- [23] N. Berrah, A perspective for investigating photo-induced molecular dynamics from within with femtosecond free electron lasers, Phys. Chem. Chem. Phys. 19, 19536 (2017).
- [24] F. Bencivenga, F. Capotondi, E. Principi, M. Kiskinova, and C. Masciovecchio, Coherent and transient states studied with extreme ultraviolet and x-ray free electron lasers: Present and future prospects, Adv. Phys. 63, 327 (2014).

- [25] A. Rudenko *et al.*, Femtosecond response of polyatomic molecules to ultra-intense hard x-rays, Nature (London) 546, 129 (2017).
- [26] L. Funke *et al.*, Capturing nonlinear electron dynamics with fully characterised attosecond x-ray pulses, arXiv: 2408.03858.
- [27] D. Ratner, J. P. Cryan, T. J. Lane, S. Li, and G. Stupakov, Pump-probe ghost imaging with SASE FELs, Phys. Rev. X 9, 011045 (2019).
- [28] D. E. Rivas *et al.*, High-temporal-resolution x-ray spectroscopy with free-electron and optical lasers, Optica 9, 429 (2022).
- [29] A. tul noor *et al.*, Sub-50 fs temporal resolution in an FEL-optical laser pump-probe experiment at FLASH2, Opt. Express **32**, 6597 (2024).
- [30] J. M. Glownia, K. Gumerlock, H. T. Lemke, T. Sato, D. Zhu, and M. Chollet, Pump–probe experimental methodology at the Linac Coherent Light Source, J. Synchrotron Radiat. 26, 685 (2019).
- [31] C. Conti, A. Fratalocchi, G. Ruocco, and F. Sette, Nonlinear optics in the x-ray regime: Nonlinear waves and self-action effects, Opt. Express 16, 8324 (2008).
- [32] Z. Guo et al., Experimental demonstration of attosecond pump-probe spectroscopy with an x-ray free-electron laser, arXiv:2401.15250.
- [33] N. Rohringer, X-ray Raman scattering: A building block for nonlinear spectroscopy, Phil. Trans. R. Soc. A 377, 20170471 (2019).
- [34] K. Tamasaku, E. Shigemasa, Y. Inubushi, I. Inoue, T. Osaka, T. Katayama, M. Yabashi, A. Koide, T. Yokoyama, and T. Ishikawa, Nonlinear spectroscopy with x-ray two-photon absorption in metallic copper, Phys. Rev. Lett. 121, 083901 (2018).
- [35] I. Schlichting and J. Miao, Emerging opportunities in structural biology with x-ray free electron lasers, Curr. Opin. Struct. Biol. **22**, 613 (2012).
- [36] C. E. Blanchet *et al.*, Form factor determination of biological molecules with x-ray free electron laser small-angle scattering (XFEL-SAS), Commun. Biol. **6**, 1057 (2023).
- [37] A. Magunia *et al.*, Time-resolving state-specific molecular dissociation with XUV broadband absorption spectroscopy, Sci. Adv. **9**, eadk1482 (2023).
- [38] C. Behrens, F.-J. Decker, Y. Ding, V. A. Dolgashev, J. Frisch, Z. Huang, P. Krejcik, H. Loos, A. Lutman, T. J. Maxwell, J. Turner, J. Wang, M.-H. Wang, J. Welch, and J. Wu, Few femtosecond time-resolved measurements of x-ray free electron lasers, Nat. Commun. 5, 3762 (2014).
- [39] R. Akre, L. Bentson, P. Emma, and P. Krejcik, A transverse rf deflecting structure for bunch length and phase space diagnostics, in *Proceedings of the 19th Particle Accelerator Conference, Chicago, IL, 2001* (IEEE, Piscataway, NJ, 2001), Vol. 3, pp. 2353–2355, 10.1109/PAC .2001.987379.
- [40] F. Christie, A. A. Lutman, Y. Ding, Z. Huang, V. A. Jhalani, J. Krzywinski, T. J. Maxwell, D. Ratner, J. Rönsch-Schulenburg, and M. Vogt, Temporal x-ray reconstruction using temporal and spectral measurements at LCLS, Sci. Rep. 10, 9799 (2020).

- [41] J. Rossbach, J. R. Schneider, and W. Wurth, 10 years of pioneering X-ray science at the Free-Electron Laser FLASH at DESY, Phys. Rep. 808, 1 (2019).
- [42] M. Beye and S. Klumpp, FLASH202+ -Upgrade of FLASH: Conceptual Design Report (Verlag Deutsches Elektronen-Synchrotron, Hamburg, 2020), https://bib-pubdb1.desy.de/record/434950.
- [43] G. L. Orlandi, Bunch compressor monitors for the characterization of the electron bunch length in a Linac-driven FEL, in *Proceedings of the 12th International Beam Instrumentation Conference (IBIC2023)*, Saskatoon, Canada (JACoW, Geneva, Switzerland, 2023), TUP026, 10.18429/JACoW-IBIC2023-TUP026.
- [44] C. Gerth and N. Lockmann, Bunch compression monitor based on coherent diffraction radiation at European XFEL and FLASH, in *Proceedings of the 10th International Beam Instrumentation Conference (IBIC2021), Pohang, Republic of Korea* (JACoW, Geneva, Switzerland, 2021), WEPP14, 10.18429/JACoW-IBIC2021-WEPP14.
- [45] J. Breunlin, Commissioning of an electro-optic electron bunch length monitor at FLASH, Master's thesis, Hamburg University, 2011.
- [46] S. Pfeiffer, Ł. Butkowski, M. K. Czwalinna, B. Dursun, C. Gerth, B. Lautenschlager, H. Schlarb, and Ch Schmidt, Longitudinal intra-train beam-based feedback at FLASH, in *Proceedings of the 39th Free Electron Laser Conference (FEL'19), Hamburg, Germany* (JACoW, Geneva, Switzerland, 2019), pp. 346–349, 10.18429/JACoW-FEL2019-WEP011.
- [47] F. Loehl *et al.*, Measurement and stabilization of the bunch arrival time at FLASH, Conf. Proc. C **0806233**, THPC158 (2008), https://inspirehep.net/literature/795996.
- [48] M. Viti, M. Czwalinna, H. Dinter, C. Gerth, K. Przygoda, R. Rybaniec, and H. Schlarb, The bunch arrival time monitor at FLASH and European XFEL, in *Proceedings* of the 16th International Conference on Accelerator and Large Experimental Physics Control Systems (JACoW, Geneva, Switzerland, 2018), TUPHA125, 10.18429/ JACoW-ICALEPCS2017-TUPHA125.
- [49] E. Schneidmiller, M. Dreimann, M. Kuhlmann, J. Rönsch-Schulenburg, and H. Zacharias, Generation of ultrashort pulses in XUV and x-ray FELS via an excessive reverse undulator taper, Photonics 10, 653 (2023).
- [50] R. Ivanov, M. M. Bidhendi, I. J. Bermúdez Macias, M. Brachmanski, S. Kreis, S. Bonfigt, M. Degenhardt, M.-K. Czwalinna, M. Pergament, M. Kellert, F. X. Kärtner, and S. Düsterer, Free-electron laser temporal diagnostic beamline FL21 at FLASH, Opt. Express 31, 19146 (2023).
- [51] F. Christie, J. Rönsch-Schulenburg, and M. Vogt, A PolariX TDS for the FLASH2 beamline, in *Proceedings* of the 39th International Free Electron Laser Conference, Hamburg, Germany (JACoW, Geneva, Switzerland, 2019), WEP006, 10.18429/JACoW-FEL2019-WEP006.
- [52] N. S. Mirian, Longitudinal phase space of the electron beam and pulse reconstruction at FLASH (2023).
- [53] B. Marchetti et al., X-Band TDS project, in Proceedings of the 8th International Particle Accelerator Conference, Copenhagen, Denmark (JACoW, Geneva, Switzerland, 2017), 10.18429/JACoW-IPAC2017-MOPAB044.

- [54] P. Craievich et al., Status of the Polarix-TDS project, in Proceedings of the 9th International Particle Accelerator Conference, Vancouver, BC, Canada (JACoW, Geneva, Switzerland, 2018), 10.18429/JACoW-IPAC2018-THPA L068.
- [55] P. Craievich *et al.*, Novel *x*-band transverse deflection structure with variable polarization, Phys. Rev. Accel. Beams **23**, 11201 (2020).
- [56] P. González Caminal et al., Beam-based commissioning of a novel x-band transverse deflection structure with variable polarization, Phys. Rev. Accel. Beams 27, 032801 (2024).
- [57] T. Wilksen, A. Aghababyan, L. Fröhlich, O. Hensler, R. Kammering, K. Rehlich, and V. Rybnikov, A bunch-synchronized data acquisition system for the European XFEL accelerator, in *Proceedings of the 16th International Conference on Accelerator and Large Experimental Physics Control Systems* (JACoW, Geneva, Switzerland, 2018), TUPHA210, 10.18429/JACoW-ICALEPCS2017-TUPHA 210.
- [58] N. Otsu, A threshold selection method from gray-level histograms, IEEE Trans. Syst. Man Cybern. 9, 62 (1979).
- [59] R. Haase, A. Jain, S. Rigaud, D. Vorkel, P. Rajasekhar, T. Suckert, T. J. Lambert, J. Nunez-Iglesias, D. P. Poole, P. Tomancak, and E. W. Myers, Interactive design of GPU-accelerated image data flow graphs and cross-platform deployment using multi-lingual code generation, biorXiv (2020), 10.1101/2020.11.19.386565.
- [60] S. Rigaud, R. Haase, C. Latechre, J. Soltwedel, M. Albert, P. Rajasekhar, and G. Ross, clEsperanto/pyclesperanto (2024), https://github.com/clEsperanto/pyclesperanto.
- [61] T. Akiba, S. Sano, T. Yanase, T. Ohta, and M. Koyama, Optuna: A next-generation hyperparameter optimization framework, in *Proceedings of the 25th ACM SIGKDD International Conference on Knowledge Discovery & Data Mining, KDD '19* (Association for Computing Machinery (ACM), New York, NY, 2019), pp. 2623–2631, 10.1145/3292500.3330701.
- [62] J. Ansel et al., PyTorch 2: Faster machine learning through dynamic Python Bytecode transformation and graph compilation, in Proceedings of the 29th ACM International Conference on Architectural Support for Programming Languages and Operating Systems (ACM, New York, NY, 2024), Vol. 2, 10.1145/3620665.3640366.
- [63] D. P. Kingma and J. Ba, Adam: A method for stochastic optimization, arXiv:1412.6980.
- [64] W. Falcon and The PyTorch Lightning team, PyTorch lightning (2019), 10.5281/zenodo.3828935.
- [65] F. Wilcoxon, Individual comparisons by ranking methods, Biometrics Bull. 1, 80 (1945).
- [66] C. Bonferroni, Teoria statistica delle classi e calcolo delle probabilita, Pubblicazioni del R istituto superiore di scienze economiche e commericiali di firenze **8**, 3 (1936), https://cir.nii.ac.jp/crid/1570009749360424576.
- [67] J. W. Tukey, Comparing individual means in the analysis of variance, Biometrics 5, 99 (1949).
- [68] S. Roling, B. Siemer, M. Wöstmann, H. Zacharias, R. Mitzner, A. Singer, K. Tiedtke, and I. A. Vartanyants, Temporal and spatial coherence properties of free-electron-laser pulses in the extreme ultraviolet regime, Phys. Rev. ST Accel. Beams 14, 080701 (2011).